American Mineralogist, Volume 111, pages 231–245, 2026

Quartz-petalite intergrowths in the Yichun pegmatite: Formation from late-stage Li-rich melts and implications for Li mineralization in rare-metal granites

Mingqian Wu[1,2,3,*], Iain M. Samson[3], Anouk M. Borst[4,5], Xi Diao[1,†], Charles D. Beard[6], Xu Zheng[7], Mei Fan[1], Zhaoliang Hou[1,‡], and Kunfeng Qiu[1,8,*]

[1]State Key Laboratory of Geological Processes and Mineral Resources, School of Earth Sciences and Resources, China University of Geosciences, Beijing 100083, China
[2]Key Laboratory of Metallogenic Geological Process and Resources Utilization in Shandong Province, Key Laboratory of Gold Mineralization Processes and Resource Utilization Subordinated to the Ministry of Natural Resources, Shandong Institute of Geological Sciences, Jinan 250013, China
[3]School of the Environment, University of Windsor, Windsor, Ontario N9B 3P4, Canada
[4]Department of Earth and Environmental Sciences, KU Leuven, Celestijnenlaan 200E, Heverlee 3001, Belgium
[5]Section of Geodynamics and Mineral Resources, Royal Museum for Central Africa, Tervuren 3080, Belgium
[6]Department of Earth Sciences, Utrecht University, 3584 CB Utrecht, The Netherlands
[7]Institute of Geology, Chinese Academy of Geological Sciences, Beijing 100037, China
[8]Frontiers Science Center for Deep-time Digital Earth, China University of Geosciences, Beijing 100083, China

Abstract

We report a unique quartz-petalite intergrowth that occurs in the core zone of a zoned pegmatite sheet from the Yichun Li-Cs-Ta-Nb mine, China. Within this deposit, a rare-metal-mineralized granite underlies and partially intrudes into the earlier, zoned pegmatite, both of which have previously been interpreted to have originated from the same parental magma. The pegmatite core zone mostly comprises an early quartz generation that is fractured and free of mineral inclusions. A less abundant later quartz partially replaced the early quartz and is characterized by abundant globular to vermicular inclusions of petalite ($LiAlSi_4O_{10}$) and lesser K-feldspar (orthoclase/sanidine). These two types of sequentially crystallized quartz have $\delta^{18}O$ values (12.7–13.0‰) similar to magmatic graphic quartz in the pegmatite wall zone. Hydrothermal quartz in later veins has higher $\delta^{18}O$ (13.7–14.2‰). Titanium-in-quartz thermobarometry indicates similar crystallization temperatures (ca. 500 °C) for both quartz generations. Textural features and mass-balance calculations suggest that most petalite inclusions formed by exsolution from a magmatic quartz-petalite solid solution containing 1729–3135 ppm Li and >6649–12 118 ppm Al, which resembles stuffed quartz observed in experiments involving the crystallization of Li-rich granitic melts. In addition, some petalite inclusions define growth patterns indicating co-precipitation with the host quartz and represent direct crystallization from the last aliquot of pegmatite melt containing ≤5000 ppm Li. Orthoclase/sanidine inclusions formed in early quartz crystals as co-precipitates with quartz (forming micrographic textures), and later via exsolution together with petalite. To attain ~2200 ppm Li in the core zone, 90% fractionation of an initial granitic melt containing ca. 300 ppm Li is sufficient. Although the rare-metal-mineralized granite at Yichun was suggested to have originated from a melt of similar compositions to the initial granitic melt that formed the pegmatite, the up to 1.2 wt% Li in the mineralized granite cannot be achieved through similar degrees of fractional crystallization. This highlights the indispensable role of metasomatism in the formation of economic-grade, granite-hosted Li mineralization at Yichun and, possibly, in analogous systems.

Keywords: Lithium mineralization, mineral morphology and structure, quartz-petalite solid solution, exsolution, chemical and isotope features of quartz, Rayleigh fractionation

Introduction

Lithium-rich peraluminous granites and pegmatites have received global attention in exploration and research due to the strategic importance of Li in green technologies, in particular Li-ion batteries (e.g., Kesler et al. 2012; Černý et al. 2012; London 2016; Bradley et al. 2017; Bowell et al. 2020; Kerr 2023). South China is world-renowned for its large endowment of Li, primarily as Li-rich mica (i.e., lepidolite and zinnwaldite) in peraluminous rare-metal Li-mica granites (Li et al. 2015; Wu et al. 2017, 2018, 2024; Zhu et al. 2018). These Li-rich granites are commonly overlain by thin sheets or dikes of pegmatite (Yin et al. 1995; Zhu et al. 2001; Diao et al. 2022; Guo et al. 2024), but the latter are less economically significant due to their relatively small size and lower abundance of rare-metal minerals compared to the underlying granites, or compared to economically mineralized rare-metal pegmatites elsewhere (e.g., Tanco, Canada and Bikita, Zimbabwe) (Dittrich et al. 2019; London 2024). Both experimental work and field-based studies suggest that low-degree partial melting of metasediments, coupled with

* Co-corresponding author E-mails: aria.wu@uwindsor.ca Orcid https://orcid.org/0000-0002-2041-6623, kunfengqiu@qq.com
† Orcid https://orcid.org/0000-0002-7347-5598
‡ Orcid https://orcid.org/0000-0003-4937-2940

0003-004X/26/0002–231$05.00/DOI: https://doi.org/10.2138/am-2025-9818

prolonged magmatic evolution, can produce rocks that are compositionally similar to the South China rare-metal granites and their overlying pegmatites (e.g., Černý et al. 2005; Linnen and Cuney 2008; Pollard 2021). For example, for the Yichun deposit, which is currently being mined for lithium, Yin et al. (1995) suggested that the zinnwaldite-muscovite granite, which is the lowermost unit exposed at the surface, was derived from low-degree partial melting of metasediments and progressively evolved, through fractional crystallization, to a Li-muscovite granite, a Li-Cs-Ta-Nb-mineralized topaz-lepidolite granite, and finally to a pegmatite at the top. This model is in line with most publications about the South China granites, where the pegmatites are regarded as marginal pegmatites (i.e., stockscheiders) (cf. Breiter et al. 2005) and are interpreted to represent the final crystallization products of the melts that crystallized the underlying granites (e.g., Lin 1996; Zhu et al. 2001; Wu et al. 2018). However, the observation that most of these presumably late, more fractionated pegmatites contain lower rare-metal contents, particularly Li, than their underlying, supposedly less-fractionated granites is inconsistent with the above model. In addition, field relationships at Yichun, where the pegmatite is crosscut by, and therefore earlier than, the underlying topaz-lepidolite granite (Pollard 2021; Wu et al. 2024), do not fit with the model.

To explain this field observation and the compositional gap between the topaz-lepidolite granite and underlying granites, Pollard (2021) suggested that constitutional zone refining, a magmatic boundary layer effect, played a significant role in locally concentrating rare metals at Yichun and led to economic mineralization within both the granite and pegmatite bodies. A different model was proposed by Wu et al. (2018, 2024), in which the economic ore bodies (the topaz-lepidolite granite and parts of the pegmatite) are those that underwent the most extensive metasomatism, based on: (1) the resorption and overgrowths of Ta oxides over columbite-(Mn) crystals; (2) the abundance of Li-rich pseudomorphs in the mineralized parts of the granite-pegmatite system; and (3) the comparable compositions of lepidolite disseminated in the granites to lepidolite from the miarolitic cavities, veins, and pseudomorphs that are of undoubtedly metasomatic origin. Importantly, it was recently hypothesized that the pegmatites of rare-metal granites in South China were emplaced first and subsequently acted as permeability barriers, leading to protracted magmatic-hydrothermal evolution in the younger granites, by inhibiting their degassing (Michaud and Pichavant 2020; Guo et al. 2024). A prolonged magmatic-hydrothermal evolution would allow a late rare-metal granite to "stew in its own juices," promoting intense (auto) metasomatism, which is believed by many as an indispensable stage for economic rare-metal mineralization, especially Li enrichment, in rare-metal granites (Zhu et al. 2015; Ballouard et al. 2016, 2020; Harlaux et al. 2017; Wu et al. 2017, 2018, 2024; Diao et al. 2022, 2024). The debates described above call for continued investigation into whether Li mineralization in the South China rare-metal granites can be achieved solely by magmatic processes.

At Yichun, many parts of the pegmatite are suggested to have preserved magmatic characteristics and are unaffected by metasomatic alteration, contrasting to the directly underlying topaz-lepidolite granite that underwent extensive metasomatism (Wu et al. 2018, 2024; Pollard 2021). These preserved parts include a quartz-dominant core zone (i.e., the most evolved part of a zoned pegmatite in terms of igneous evolution) that contains petalite ($LiAlSi_4O_{10}$) inclusions. They therefore record the enrichment of Li via magmatic fractionation, without subsequent metasomatic modification. Because these unaltered pegmatite parts and all the exposed granite units are thought to have derived from a common magma at depth, we use the pegmatite record to explore magmatic processes that have similarly affected the underlying granite (Pollard 2021; Yin et al. 2022; Wu et al. 2024). By comparing Li concentrations in the unaltered parts of the pegmatite with those in the underlying topaz-lepidolite granite, we can evaluate to what extent metasomatism contributed to the Li mineralization in the topaz-lepidolite granite relative to its initial magmatic Li enrichment. The results may be relevant to other analogous systems in South China or elsewhere.

Geology of the Yichun Deposit

The Yichun deposit, located in South China, is situated within the vertically zoned Yashan granite complex that outcrops over ca. 9.5 km^2. The three main rock units have gradational contacts and are, from bottom to top, a zinnwaldite-muscovite granite, a Li-muscovite granite, and a Li-Cs-Ta-Nb-mineralized topaz-lepidolite granite (Fig. 1). Several leucogranitic dikes that crosscut both the Li-muscovite and topaz-lepidolite granites are invariably kaolinized, such that their original mineralogy is uncertain; concealed muscovite granites are reported from drill core that is no longer available (Yin et al. 1995; Huang et al. 2002) (Fig. 1). Zircon and columbite-group minerals collected from the zinnwaldite-muscovite granite (Lou et al. 2005) and topaz-lepidolite granite (Che et al. 2015), respectively, yielded comparable U-Pb isotopic ages of ca. 160 Ma, suggesting that the emplacement of the Yashan complex is approximately coeval with its contained Ta mineralization. Wu et al. (2024) recently proposed that the topaz-lepidolite granite represents the extensively metasomatized product of what was previously the upper portion of the Li-muscovite granite. A tabular pegmatite body, which is ~96 000 m^3 in size (400 × 60 × 4 m), is crosscut by, and thus predates, the underlying topaz-lepidolite granite (Pollard 2021; Wu et al. 2024). The pegmatite is internally zoned (Fig. 2a) and consists of three main zones from bottom to top, namely a graphic-textured wall zone, a UST-textured intermediate zone, and a core dominated by quartz (Fig. 2b) that is crosscut by abundant thin veins comprising albite, lepidolite, cookeite, and quartz [described as the ALC veins in Wu et al. (2024)]. Graphic quartz crystals in the wall zone are several to a few millimeters in size and embedded in albite aggregates (Online Materials[1] Fig. S1) or larger K-felspar crystals; in pegmatites, such graphic quartz is of magmatic origin (cf. Fenn 1986; London 2008; Baker et al. 2018). The ALC veins (Fig. 3a; cf. Wu et al. 2024), which contain minor quartz crystals, on the other hand, are interpreted as hydrothermal. The metasediments occur in contact with the core zone at the southeast end of the exposed pegmatite (Fig. 1). Given that core zones occur, in general, in the center of zoned pegmatite bodies (e.g., London 2008, 2018), the absence of any wall or intermediate zones above the exposed core

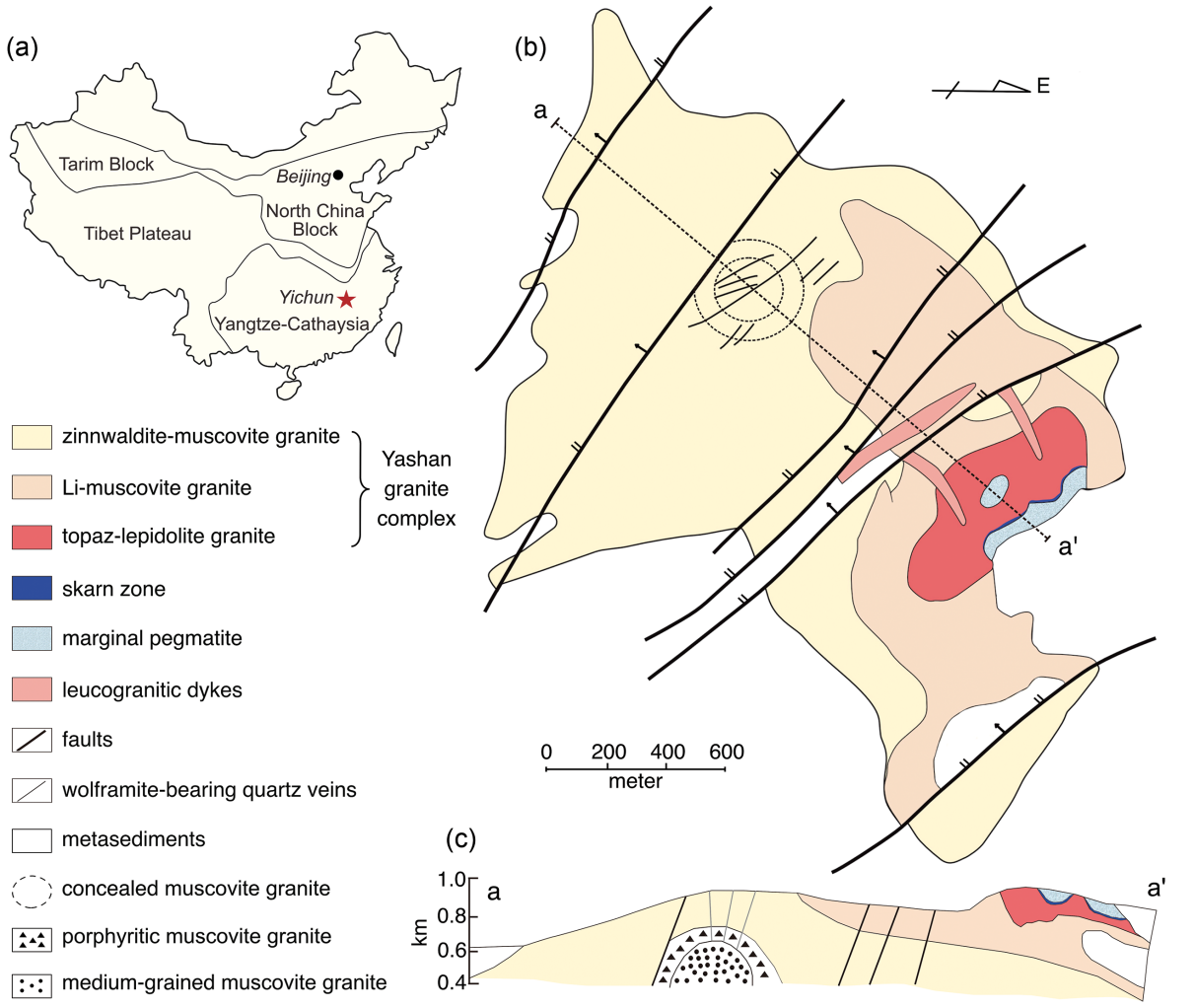

Figure 1. (**a**) Location of the Yichun deposit in the Cathaysia Block, Southeastern China. (**b**) Simplified geological map of the Yichun deposit showing a plan view of the deposit, and (**c**) the a-a′ cross section through the deposit. Note that the leucogranitic dikes are not illustrated in (**c**), as their spatial distribution is poorly constrained (modified after Yin et al. 1995). (Color online.)

suggests that the topmost parts of the pegmatite have been eroded away and that the metasediments in contact with the core zone (Fig. 2) represent an enclave of country rocks.

Methods

Thin and thick sections were made from 20 samples collected from different localities of the pegmatite core zone for textural and chemical analyses. A series of instruments was used for optical examination of petrographic characteristics, including an Epson Perfection V850 Pro scanner, in which sections were sandwiched between two polarizing films during scanning, a binocular microscope, and an Olympus BX 51 polarizing microscope.

Mineral identification and imaging were conducted at the Centre for Advanced Microscopy and Materials Characterization at the University of Windsor, Canada. An FEI Quanta 200 FEG environmental scanning electron microscope (SEM) paired with an EDAX Octane Plus energy-dispersive spectrometric (EDS) or a Centaurus cathodoluminescence (CL) detector and a WITec Alpha 300 Raman spectrometer with a 532-nm air-cooled argon-ion laser were used. The SEM instrument was operated in high-vacuum mode with a 15 kV accelerating voltage, a 30 nA beam current, and a 1.5 µm beam diameter for backscattered electron (BSE) imaging and EDS analysis. For CL images, the SEM was operated in high-vacuum mode with an accelerating voltage of 15 kV, a beam current of 20 nA, and a 1.5 µm beam diameter. Laser Raman spectroscopy was used to identify the minerals enclosed in quartz. A WITec Alpha 300 Raman spectrometer with a 532 nm air-cooled argon-ion laser was used. The output laser power was set to close to 50 mW, and a 100× objective lens was used to focus the laser. The obtained Raman spectra were batch processed using the WiTec Project Plus software. Two varieties of mineral inclusions, namely petalite and K-feldspar, were identified and will be described in detail in the Results section.

Image analysis was conducted on SEM-CL images, each of which is of 2048 × 1887 pixels. The obtained CL images were used to visualize the distribution of the different generations of quartz and the petalite and K-feldspar mineral inclusions it contains. The significant brightness difference of globular petalite (bright) relative to quartz (gray) and K-feldspar/cracks (both dark) allows quantitative analysis of the concentration of petalite inclusions in quartz. Image processing was performed using Fiji ImageJ (Schneider et al. 2012). The images were converted to an 8-bit mode and denoised with a median filter with a pixel radius of 1 (Hou et al. 2023, 2024). To analyze the area of petalite in a selected domain, sub-images of these domains from each image were extracted, according to a rationale of the size of petalite inclusions, where domains containing mainly >50 µm and <20 µm inclusions, respectively, can be identified. Petalite was segmented from quartz and K-feldspar/cracks using the "Threshold" function. The concentration density of petalite was analyzed by calculating its area divided by the unit area using the "Fraction" function.

To determine the trace-element concentrations of quartz, laser ablation inductively coupled plasma mass spectrometry (LA-ICP-MS) was carried out at the

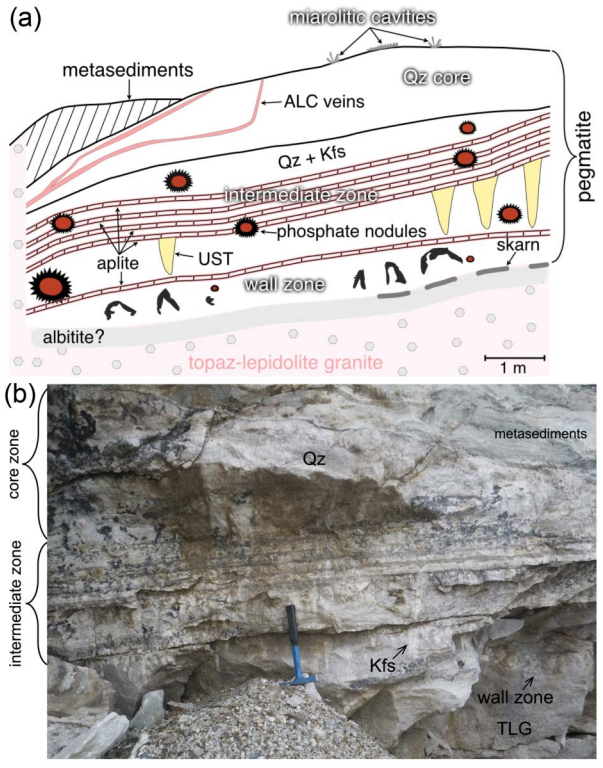

Figure 2. (**a**) Schematic cross section showing the general distribution of each zone in the pegmatite (modified after Wu et al. 2018, 2024) and the topaz-lepidolite granite crosscutting the pegmatite. (**b**) Representative photograph of the cross section of a part of the pegmatite, sandwiched between metasedimentary rocks at the top and the topaz-lepidolite granite at the bottom. The hammer shown in this photo is about 20 cm in length. Note that this cross section shows only the three main zones of the pegmatite. UST = unidirectional solidification textures; ALC = albite-lepidolite-cookeite; TLG = topaz-lepidolite granite; Qz = quartz; Kfs = K-feldspar. (Color online.)

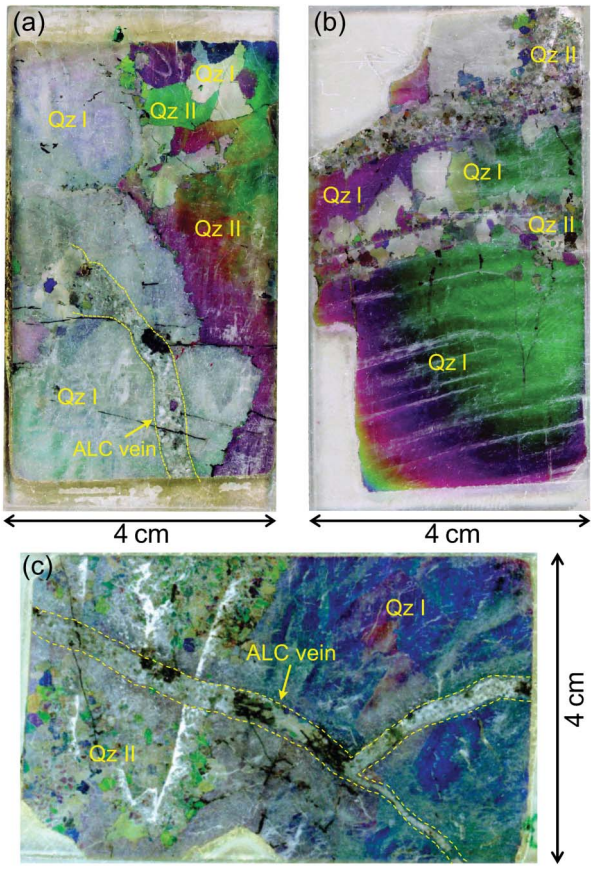

Figure 3. (**a**–**c**) Scanned thick (100–120 µm) sections in partially cross-polarized light showing the distribution of the two generations of quartz (Qz I and II) in core zone samples. The albite-lepidolite-cookeite (ALC) veins, as shown in (**a**) and (**c**), crosscut quartz of both generations. (Color online.)

Uranium-Polymetallic Research Center, State Key Laboratory of Nuclear Resources and Environment in the East China University of Technology. The LA-ICP-MS comprises PerkinElmer NexION 1000 quadrupole ICP-MS coupled with an ESI NWR 257 femtosecond pulse excimer laser system, operating at a wavelength of 257 nm. The energy density and repetition rate were set at 2.3 J/cm^2 and 8 Hz, respectively. Laser ablation was performed in spots with a width of ~40 µm. The acquisition time was set to 50–60 s, including a 45 s acquisition for the helium gas background. Every 5–8 analyses were followed by two analyses of the NIST 610 and 612 synthetic glass standards for time-dependent calibration of sensitivity drift. The following masses were measured, and the resulting average detection limits for each element's concentration are reported in parts per million (in parentheses): ^{7}Li (0.30), ^{27}Al (0.80), ^{29}Si (517), ^{47}Ti (0.21), and ^{49}Ti (0.46). Quantitative concentrations of these elements were calculated using NIST 610 as the external reference standard and a Si concentration of 46.7 wt% (assuming stoichiometric Si contents in quartz) as the internal standard. The Iolite 4 software was used for raw data processing, including sample and background signal determinations, drift calibrations, and element concentration calculations (Paton et al. 2011). Titanium-in-quartz thermometric calculations were conducted using measured Ti concentrations in quartz (an average of the sum of ^{47}Ti and ^{49}Ti), adopting log Ti (ppm) = $-0.27943 \times 10^4/T - 660.53 \times (P^{0.35}/T) + 5.6459$ at certain pressures, an equation proposed by Huang and Audétat (2012). For data comparison and test of this algorithm on the studied system, magmatic graphic quartz crystals from the wall zone of the pegmatite were analyzed using the same workflow described above. The data are listed in the Online Materials[1] Table S1. It is worth noting that, amidst a plethora of Ti-in-quartz thermometers, we opted for this algorithm because it is calibrated for application to magmatic systems and does not require parameter adjustments depending on the presence or absence of primary Ti-phases (to constrain TiO_2 activity) in the system, thereby eliminating the potential influence of calculation results by petrological observations.

Sections used for the above analyses were also chosen for in situ quartz oxygen isotope analyses using a SHRIMP II MC at the Beijing SHRIMP Center, Chinese Academy of Geological Sciences, or the Shandong SHRIMP Center, Shandong Institute of Geological Sciences. Disks containing the target quartz grains were drilled out directly from these sections to meet the requirements for sample size. The disks were then mounted, polished, and plated with gold prior to O isotope analyses. The analyses were carried out following the analytical procedures described by Wei et al. (2024). The accelerating voltage was set to 10 kV, and a Cs^+ beam was focused to a 25 × 30 µm spot on the sample surface, with a primary current of ~5 nA. The analyses were performed on the same grains used for SEM-CL. Although duplicating the same spots chosen for LA-ICP-MS analyses is not possible, we conducted oxygen isotope analyses on adjacent domains with similar textural features. The ^{16}O and ^{18}O isotopes were measured in a multi-collector mode by quadruple Faraday cups. The δ^{18}O values are referenced to the Vienna standard mean ocean water (VSMOW, $^{18}O/^{16}O = 0.0020052$), and uncertainties for individual analyses are at a 2σ confidence level. A 90 s pre-analysis sputtering was used to remove the high-purity gold layer, followed by an ~90 s secondary ion centering and mass calibration. The signals were measured in a 320 s accumulation session, which consists of 20 cycles of measurements, and each cycle contains 1 s of waiting time and 15 s of counting time. The total analytical time of a single spot was ~8.5 min. NBS28, whose δ^{18}O values (9.57 ± 0.12‰) were stable throughout the experiment, was analyzed for calibration of δ^{18}O values after every 2 analyses. The δ^{18}O values of NBS28 were stable and reproducible during analyses. Quartz from the core zone,

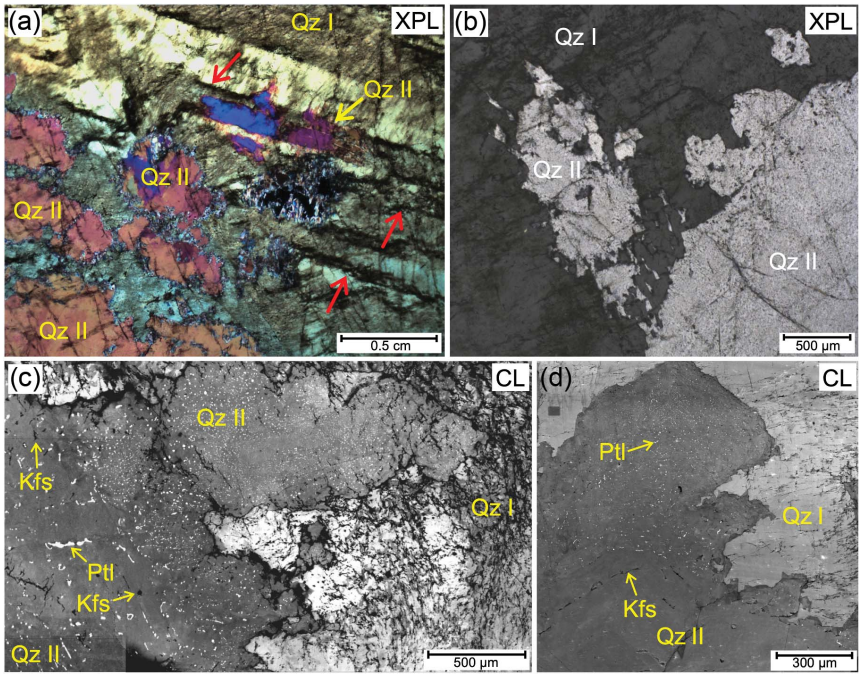

Figure 4. (**a**) Quartz II as replacement patches along growth zones (red arrows) in Qz I (thick section). (**b**) An optical photomicrograph showing that the first generation of quartz (Qz I) exhibits optical discontinuity with the second generation of quartz (Qz II), where Qz II resorbed Qz I (thin section). Note that Qz II appears more pixelated than Qz I as it contains numerous mineral inclusions that are not present in Qz I. (**c**) Scanning electron microscope-cathodoluminescence (SEM-CL) photo showing the different luminescent features of Qz I and II, and that the K-feldspar and petalite inclusions exhibit different CL responses. (**d**) An SEM-CL image illustrates the presence of both dark K-feldspar and bright petalite mineral inclusions in Qz II, and the embayment of Qz I by Qz II. The small gray box in (**d**) is an area damaged by the electron beam during focus optimization of the image. XPL = Cross-polarized light; CL = SEM-CL; Ptl = petalite. (Color online.)

magmatic graphic quartz from the wall zone, and hydrothermal quartz from the ALC veins were analyzed. The data are listed in Online Materials[1] Table S2.

Results

Textures of the Pegmatite Core Zone

No minerals other than quartz have been observed in the core zone, except for mineral inclusions hosted by quartz and in the post-core, cross-cutting albite-lepidolite-cookeite (ALC) veins (Figs. 3a–3c). Two varieties of quartz have been identified using optical imaging. The first type (Qz I) accounts for >90% of the quartz in the core and comprises coarse-grained (up to 30 cm), milky, anhedral crystals (Fig. 3a) that contain abundant melt/fluid inclusions. The second type (Qz II) is clear in hand specimen and finer-grained than Qz I. It occurs as individual, millimeter-sized, anhedral to subhedral crystals or in aggregates that occur as centimeter-sized patches or veins in Qz I (Figs. 3b, 3c, and 4a). Quartz II is characterized by abundant petalite and K-feldspar inclusions, and fewer melt/fluid inclusions than Qz I, and has irregular contacts with Qz I, where the two types are in optical discontinuity (Figs. 4a and 4b). Quartz II crystals occur as replacement patches that, in some samples, cut across and have preferentially replaced along growth zones in Qz I crystals, leaving relics of Qz I within Qz II (Fig. 4a), thus requiring that Qz II postdates Qz I. The ALC veins crosscut both types of quartz (Fig. 3c). Quartz II is most commonly darker than Qz I in SEM-CL images, except when Qz I is highly fractured or particularly fluid inclusion-rich (Figs. 4c and 4d). Both Qz I and II are generally unzoned in SEM-CL images, although parts of some Qz II crystals exhibit weak oscillatory zoning (Fig. 4d).

Mineral Inclusions

As noted above, Qz II is characterized by the presence of abundant mineral inclusions. Three main types of Qz II occur that differ in the nature and character of inclusions. The first (Qz II-a) is defined by the presence of elongated or vermicular K-feldspar inclusions. These vary in abundance but, in many cases, define a micrographic texture comprising small K-feldspar crystals intergrown with the host quartz (Figs. 4d and 5a–5c). This type of Qz II occasionally develops oscillatory zoning, and in some cases the K-feldspar inclusions occur parallel to growth zones in the quartz (Fig. 5a). Raman spectra match orthoclase (RRUFF reference No. R040055) and sanidine (RRUFF reference No. R060313) (Fig. 6a) but lack the bands at 749 and 814 cm^{-1} that are characteristic of microcline (RRUFF reference No. R040154, Fig. 6a). Reference mineral Raman spectra are from Downs (2006).

Quartz II-b, which is the most abundant type of Qz II, is characterized by typically globular or vermicular inclusions of petalite. In most Qz II-b crystals, these are abundant and randomly disseminated throughout the host quartz (Figs. 4c, 4d, and 5a–5c). In many cases, Qz II-b has grown on euhedral terminations of Qz II-a, leaving well-defined boundaries between Qz II-a and -b (Figs. 5a–5c). The petalite inclusions are characterized by brighter SEM-CL luminescence than the host quartz

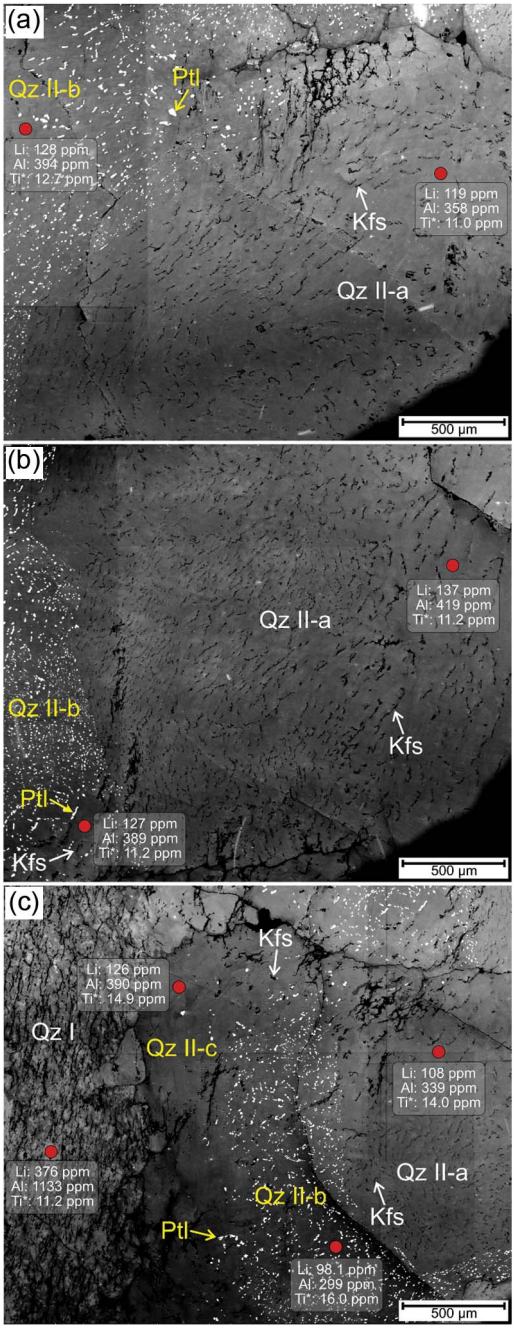

Figure 5. Representative SEM-CL photos of Qz II-a, -b, and -c. (**a**) and (**b**) Growth of petalite-bearing Qz II-b on euhedral termination of Qz II-a that contains micrographic K-feldspar inclusions. (**c**) Growth of Qz II-c as a rim on Qz II-b. The red circles and data annotations represent the spots chosen for chemical analysis and the Li, Al, and Ti* (an average of the sum of ^{47}Ti and ^{49}Ti) contents, respectively, of each spot. (Color online.)

(Figs. 4b, 4c, and 5a–5c) but have a similar BSE response (Online Materials[1] Fig. S2). EDS analyses indicate an Al:Si ratio of 1:4 and their Raman spectral characteristics are all consistent with petalite (RRUFF reference No. R040100) (Fig. 6b). The petalite inclusions vary in size, ranging from <5 to >100 µm in a single Qz II-b crystal (Figs. 4c), but are absent from Qz II-a. Although the petalite inclusions are randomly distributed through the host quartz in the majority of Qz II-b crystals, however, they exhibit different textures and distributions in some crystals. Most commonly, domains (irregular patches and elongated zones) containing coarser petalite inclusions (generally >50 µm) appear to be cutting through and surrounding areas of finer inclusions (generally 10–20 µm, but can be <5 µm), and in cases have associated dark fluid inclusions (Fig. 7a).

In some samples, petalite inclusions are not evenly and randomly disseminated through quartz, as described above, but rather their distribution appears to be related to the growth of the host quartz, after the formation of Qz II-b. Such quartz will be referred collectively as Qz II-c. The most common manifestation of this is the presence of an outer zone of Qz II-c (Figs. 5c and 7b) that contains fewer and larger petalite inclusions (commonly >100 µm in size) and that has grown on a domain of Qz II-b containing small, homogeneously distributed petalite inclusions. The boundary between Qz II-b and -c is commonly distinct and relatively sharp (Fig. 7c) but can be more gradational (Fig. 7d). This may reflect how a boundary is intersected in the sections but is more likely a result of the nature of crystal growth. In many cases, the Qz II-b domains are anhedral, but in others, the core domains are euhedral and the boundaries between the Qz II-b cores and the surrounding Qz II-c are sharp (Figs. 5c and 7b). Moreover, in crystals where the Qz II-b core is euhedral and well-defined, the boundary between the core (II-b) and outer zone (II-c) is commonly marked by the presence of dark fluid inclusions (Figs. 7b and 7e). Some Qz II-c contains petalite inclusions that are elongated in the apparent direction of Qz II-c growth (Fig. 7c) or lie parallel to (define) Qz II-c growth surfaces (Fig. 7f). Rarely, vermicular petalite inclusions form a plumose texture in Qz II-c (Fig. 7g). Qz II-c also contains some fibrous mineral inclusions (Fig. 7h) that contain roughly equal atomic amounts of Mn and P. The Raman spectra of these inclusions show a prominent peak at ~950 cm^{-1}, which is characteristic of the v1 symmetric stretching mode of PO_4^{3-} in phosphate minerals (Litasov and Podgornykh 2017) and is similar to the few published Raman spectra of lithiophilite ($LiMnPO_4$) (cf. RRUFF reference No. R100096) (Frost et al. 2013) (Online Materials[1] Fig. S3).

Image analysis was carried out on Qz II-b to determine the total area of petalite in selected domains that contain fine or coarse grains of petalite inclusions (Online Materials[1] Table S3; cf. Fig. 8 for representative examples). These analyses demonstrate that the ratio of petalite to quartz is consistent across the different domains. The amount of petalite ranges from 6.9% to 13.1% for the domains containing coarse petalite, and from 6.5% to 11.8% for the domains containing fine petalite; these yield comparable bulk compositions for the combined quartz + petalite aggregate in any selected domains (Figs. 8 and 9). Such image analysis cannot be implemented on Qz II-c, due to a dearth of homogeneously distributed petalite (cf. Figs. 5c and 7c).

Trace-Element and Oxygen Isotope Composition of Quartz

Quartz I generally contains 3 to 10 times higher Li and Al contents than the magmatic graphic quartz in the wall zone (309–469 ppm Li and 1133–2018 ppm Al in Qz I vs. 12–196 ppm

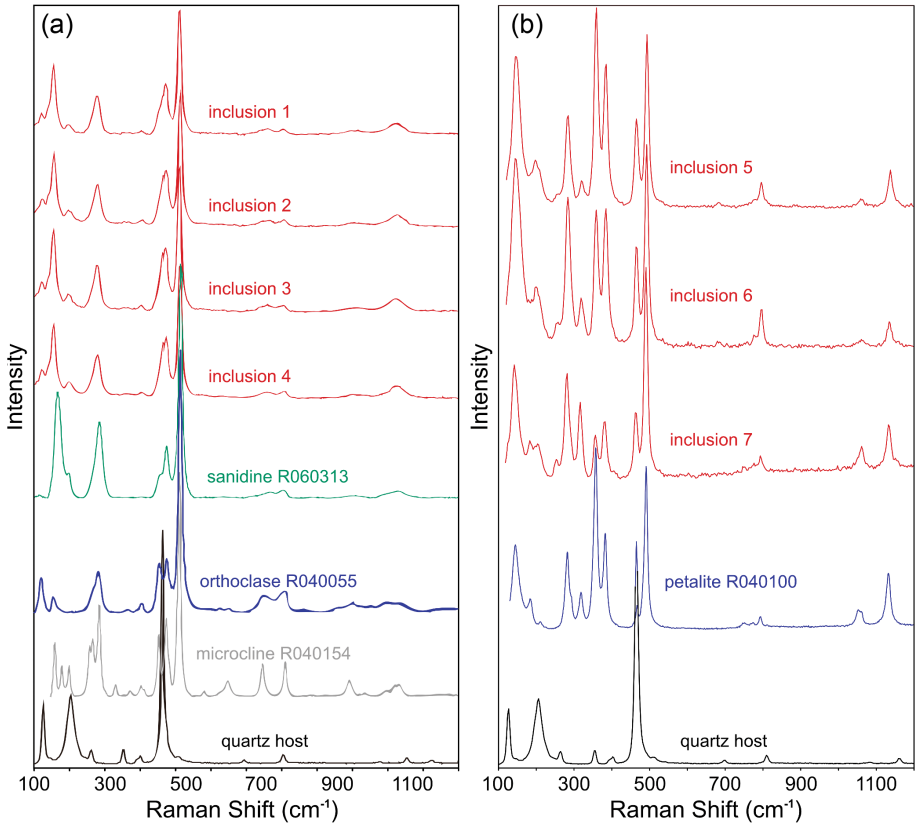

Figure 6. (**a**) Four representative Raman spectra of K-feldspar inclusions in red (the dark inclusions in SEM-CL images) with reference to representative Raman spectra of sanidine (green), orthoclase (blue), and microcline (gray). A spectrum of the host quartz is also shown. (**b**) Three representative Raman spectra of the petalite inclusions in red (the bright inclusions in SEM-CL images) with reference to a representative petalite spectrum (blue), confirming their identity as petalite. Note that more than 80 inclusions of both types were analyzed, but only seven spectra are shown for illustration. (Color online.)

Li and 66–683 ppm Al in graphic quartz) but has comparable Ti contents (Figs. 10a–10c). Quartz II exhibits similar Li, Al, and Ti concentrations to the magmatic graphic quartz (Figs. 10a–10c), and the three types of Qz II (a, b, and c) are characterized by comparable concentrations of these elements (cf. Figs. 5a–5c). Titanium-in-quartz temperatures suggest that the crystallization temperatures for Qz I are less variable than for Qz II, due to the more variable Ti contents in Qz II, although their ranges overlap: at 150 MPa, 499 to 512 °C for Qz I and 481 to 533 °C for Qz II (Fig. 10d). The graphic quartz yielded crystallization temperatures of 494–511 °C at 150 MPa that are comparable to the calculated crystallization temperatures of both Qz I and Qz II. This emplacement pressure is taken from the reported 150 MPa emplacement pressure of the underlying topaz-lepidolite granite, which is an estimate based on the initial melting temperature of melt inclusions and the homogenization temperature of fluid inclusions (Li et al. 2017). Such crystallization temperatures are comparable to the pegmatites at Bikita (Zimbabwe) and Tanco (Canada), which are estimated to have crystallized at ~450–575 and 470–650 °C, respectively (Dittrich et al. 2019; London 2024).

Quartz I and II exhibit the same range of $\delta^{18}O$ values that vary, respectively, from 12.7 to 13.0‰ and from 12.6 to 13.0‰, where the three stages of Qz II are characterized by the same oxygen isotope features. These $\delta^{18}O$ values are similar to the $\delta^{18}O$ values of the magmatic graphic quartz (12.5–13.0‰), but lower than the $\delta^{18}O$ values of the quartz from the hydrothermal ALC veins, which range from 13.7 to 14.2‰ (Fig. 11).

Discussion

Formation of the Core Zone

The core zone of the Yichun pegmatite comprises almost entirely quartz, with the exception of the mineral inclusions described above and the ALC veins that postdate the core zone (cf. Fig. 3c). It is widely accepted that quartz-dominant core zones in pegmatites are magmatic (e.g., London 2008, 2018; Simmons and Webber 2008; Bradley et al. 2017; Müller et al. 2021). This interpretation applies to the Yichun pegmatite core as both Qz I and II exhibit invariably similar $\delta^{18}O$ ranges of 12.7–13.0‰ that are comparable to those values obtained for the magmatic, graphic quartz from the same pegmatite (Fig. 11). Such ranges are within the typical $\delta^{18}O$ values of magmatic quartz from peraluminous granites that originated from partial melting of metasediments (12 to 20‰) (Bucholz et al. 2023) and are 1–1.5‰ lower than the $\delta^{18}O$ values of hydrothermal quartz from the ALC veins (Fig. 11) that crosscut both Qz I and II. Another line of evidence that suggests a magmatic origin for both Qz I and II is that their crystallization temperatures are

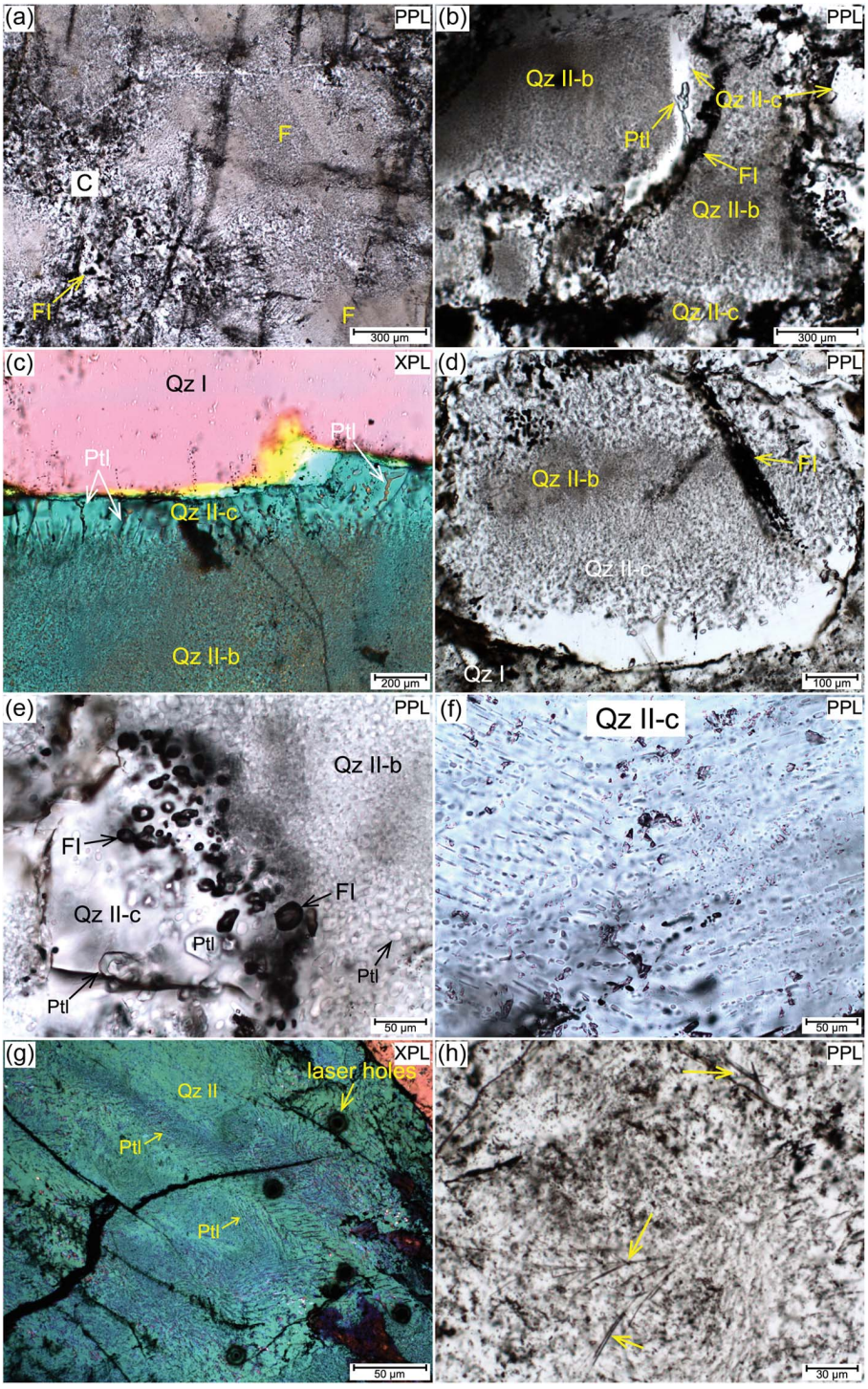

Figure 7. Transmitted light images. (**a**) Domains containing coarser inclusions (C) cutting through surrounding domains containing finer inclusions (F). Dark, vapor-rich fluid inclusions are commonly present in coarser domains and absent from the finer domains. (**b**) Quartz II-c containing large petalite inclusions that grew on euhedral aggregates of Qz II-b. (**c**) Quartz II-c that contains fewer, larger petalite inclusions grown perpendicularly to the host quartz growth surfaces, on a domain of Qz II-b containing small, homogeneously distributed petalite inclusions. The boundary between Qz II-b and -c is relatively sharp and distinct. (**d**) Quartz II-c with gradationally larger and fewer petalite inclusions occurs as surroundings to Qz II-b. Dark fluid inclusions are commonly associated with this assemblage. (**e**) Quartz II-c with petalite inclusions that have grown on the sharp termination of Qz II-b. Dark, vapor-rich fluid inclusions (Fl) are present in Qz II-c adjacent to the Qz II-b and Qz II-c boundary. (**f**) Elongated petalite inclusions oriented along putative growth surfaces of Qz II-c. (**g**) Qz II-c containing petalite inclusions forming a plumose texture. (**h**) Fibrous lithiophilite(?) crystals (yellow arrows) in Qz II-c. Note that thick sections were used for all these images to better illustrate the distribution of mineral inclusions. (Color online.)

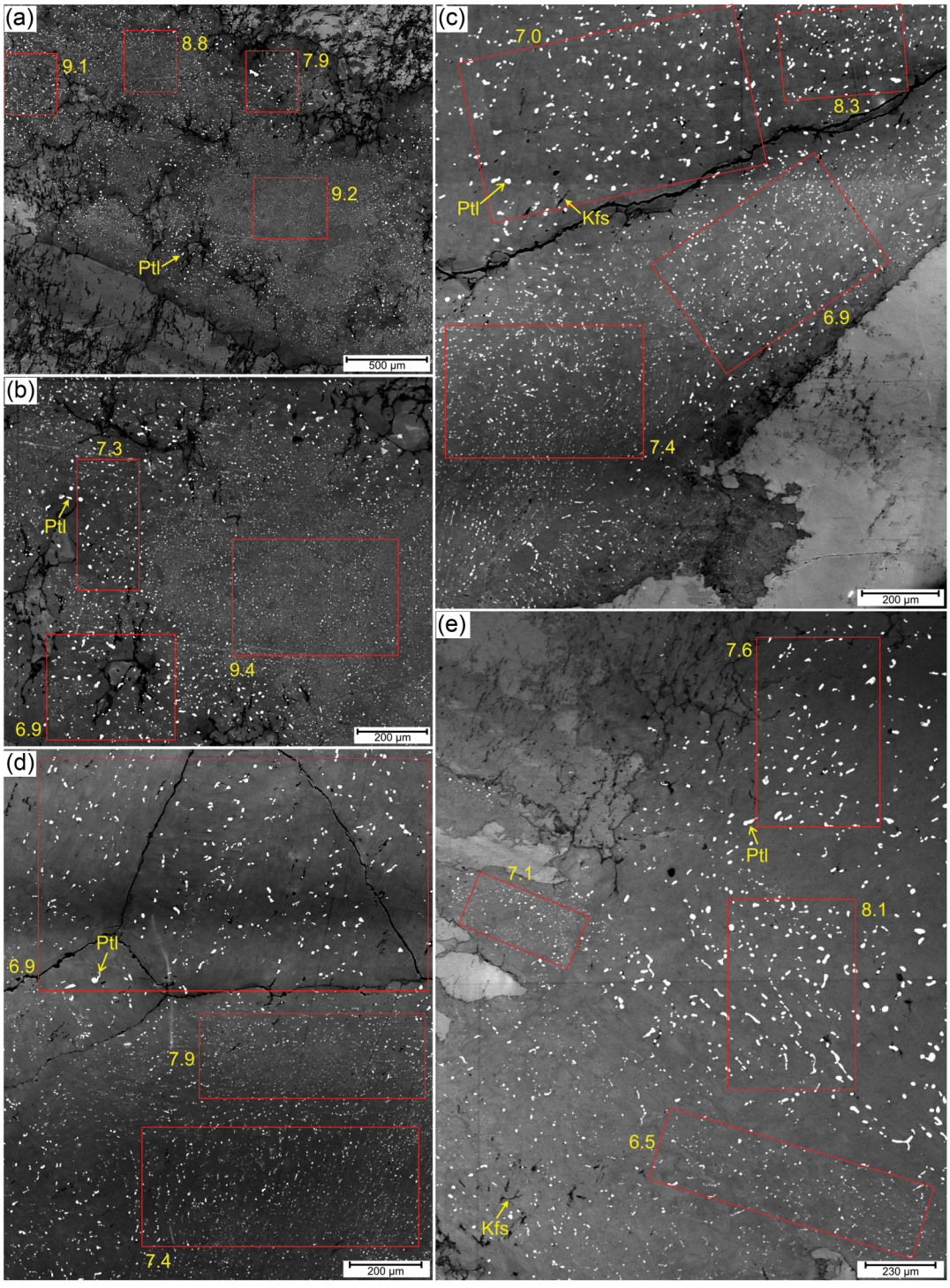

Figure 8. Representative SEM-CL images of Qz II-b crystals showing domains occupied by different sizes of petalite inclusions. The red rectangles are areas containing petalite inclusions of comparable sizes that were used to estimate the proportion of petalite using image analysis. The numbers are the petalite proportions (%) for a given rectangle. The image analysis suggests that domains occupied by petalite inclusions of different sizes are characterized by comparable amounts of petalite. (Color online.)

comparable to those for Bikita and Tanco. The magmatic origin of both Qz I and II is also consistent with the absence of low-temperature K-feldspar (i.e., microcline) (cf. Brown and Parsons 1989) (Fig. 6a) in the core zone. Therefore, Qz I constitutes the bulk of the core, whereas the subsequent crystallization of Qz II represents the last magmatic event in the pegmatite. The magmatic core was later overprinted by hydrothermal ALC veins that crosscut the magmatic quartz crystals (i.e., Quartz I and II).

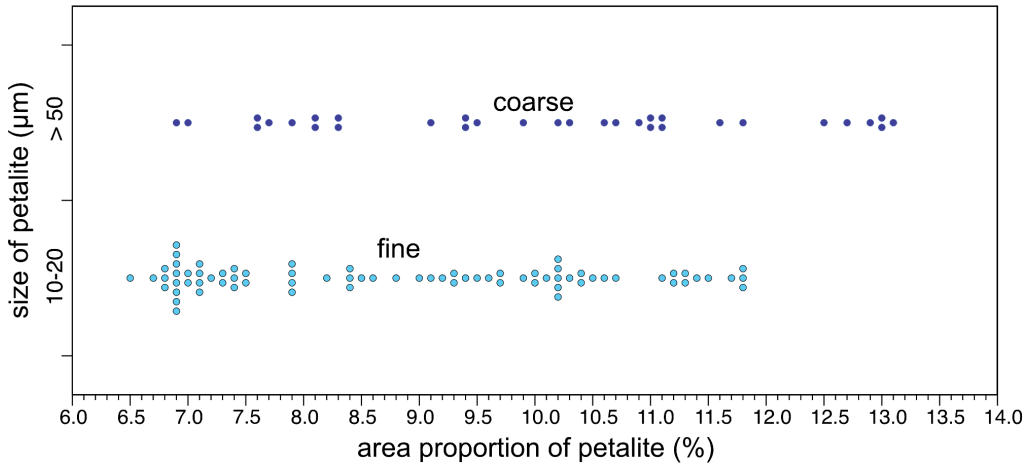

Figure 9. Area proportions of petalite for domains containing fine (~10–20 μm) and coarse (>50 μm) inclusions based on image analysis of CL images. This illustrates that domains containing the two size ranges are characterized by comparable proportions of petalite. (Color online.)

Nature of Quartz II and Its Contained Mineral Inclusions

As described above, three main stages of growth were identified in Qz II (cf. Figs. 5a–5c). The first stage is Qz II-a, which contains orthoclase/sanidine inclusions that form a micrographic texture and often defines growth zones of the host quartz. Such textures are a common magmatic feature that reflects co-precipitation of inclusion and host minerals and have been widely reported in natural pegmatites and crystallization experiments (London 2008; Baker et al. 2018; Rusiecka et al. 2020; Rusiecka and Baker 2021).

The subsequent Qz II-b contains mainly globular petalite inclusions that could either have been co-precipitated with the host quartz or formed through solid-state diffusion (i.e., exsolution). The distribution and patterns of the petalite inclusions in Qz II-c, on the other hand, strongly suggest that they were crystallized during growth of the host quartz. This is indicated by the plumose textures in some crystals (Fig. 7g), alignment of petalite inclusions perpendicular to growth surfaces in the quartz host (Fig. 7c), and the elongation of some petalite crystals in the putative direction of Qz II-c growth (Fig. 7f). We interpret the variation in size of petalite inclusions in Qz II-c to reflect varying degrees of Ostwald ripening during growth. Where growth was relatively rapid, small inclusions were formed due to limited ripening (Figs. 7f and 7g), but where growth was slow, high degrees of ripening occurred and larger petalite inclusions were formed (Figs. 7b, 7c, and 7e). The gradual increase in inclusion size outward in some crystals (Fig. 7d) is interpreted as reflecting decreasing crystal growth rates over time. The presence of lithiophilite(?) indicates that the melt contained enough P and Mn to saturate and stabilize Mn phosphates, as well as sufficient Li and Al to crystallize petalite.

A central question is how the disseminated petalite inclusions in Qz II-b were formed. Given their homogeneous and disseminated distribution, two possibilities exist: exsolution from a solid solution that crystallized from the last pegmatite melt or co-precipitation from the melt. The mineral inclusions in Qz II-b show no growth textures or relationships to growth features in the host quartz. The extremely fine-grained nature of the Qz II-b assemblage would require rapid crystallization. That rapid crystallization of the melt occurred later is indicated by the plumose textures (cf. London 2008; Sirbescu et al. 2017) in some Qz II-c (Fig. 7g). However, the euhedral nature of some Qz II-b cores (Fig. 7b) is hard to reconcile with a rapid co-precipitation model, which indicates formation of a distinct single mineral phase. Thus, an exsolution origin for Qz II-b is more likely. The homogeneous dissemination of petalite in Qz II-b and the similar calculated bulk Li and Al contents for different domains are certainly consistent with an exsolution origin, where the calculated bulk compositions reflect the solid-solution composition prior to unmixing. The calculated Li and Al contents (using the average Li and Al contents in Qz II and assuming stoichiometric petalite) in a given area (Fig. 8) mainly reflect the abundance of petalite (cf. Fig. 9). The irregular distribution of domains containing coarser inclusions than those filled with finer inclusions in Qz II-b and their association with fluid inclusions (cf. Fig. 7a), on the other hand, are not primary growth features. These are best explained by formation of the "coarser domains" through fluid-induced recrystallization of the "finer domains." The similarity of the composition of domains with larger inclusions to that of domains with finer inclusions is consistent with such an origin (Fig. 8).

The similar morphology of the globular orthoclase/sanidine and petalite inclusions in Qz II-b and the spatial association of the two minerals (cf. Figs. 5 and 8) require that the K-feldspar inclusions share the same origin as the petalite in Qz II-b. The presence and relative abundance of both petalite and orthoclase/sanidine would require that any high-temperature solid solution contained substantial Li and Al and lesser K, as well as Si and O. The image analysis calculations indicate such a solid solution would have contained ~1729–3135 ppm Li. The calculations did not include K-feldspar inclusions due to their lower abundance, so the calculated Al concentrations (6649–12 118 ppm) are minimum values.

Virgilite, a metastable solid solution between quartz and spodumene, has been found in the Macusani glass (French 1978; London and Morgan 2017) and Breasley et al. (2025)

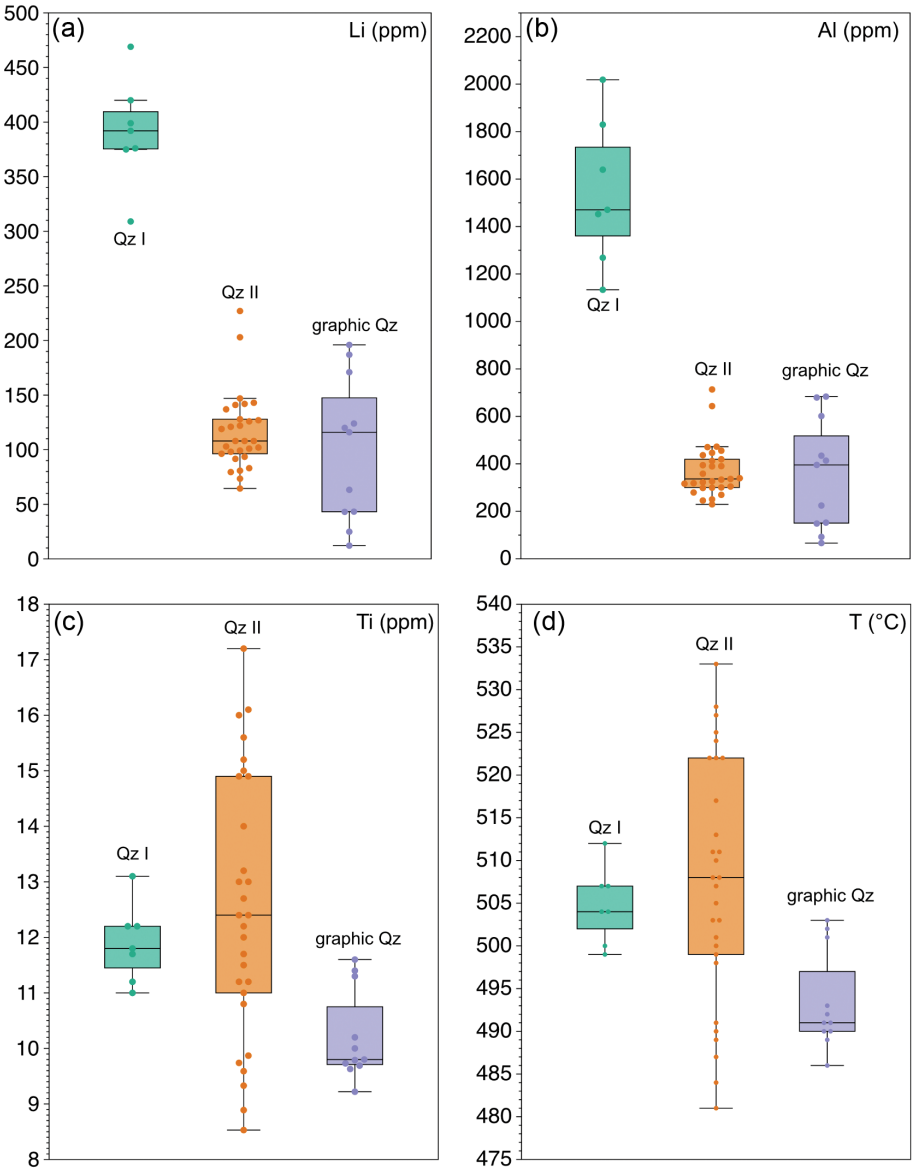

Figure 10. Box-and-whisker diagrams showing the (**a**) Li, (**b**) Al, (**c**) Ti concentrations, and (**d**) calculated titanium-in-quartz crystallization temperatures of both generations of quartz (I and II), relative to magmatic, graphic quartz (assuming a 150 MPa crystallization pressure). The lower, middle, and upper lines in each box represent the 25th, median, and 75th percentiles, respectively. The lower and upper whiskers represent the 10th and 90th percentiles, respectively. Data points below and above the 10th and 90th percentile lines represent outliers. (Color online.)

suggested that many of the spodumene-quartz intergrowths seen in the Tanco pegmatite resulted from the unmixing of virgilite precursors. One may argue that the precursor to the quartz-petalite intergrowths at Yichun is also virgilite, and the dearth of petalite at Tanco vs. the absence of spodumene in the Yichun pegmatite simply reflects the different pressures at which unmixing occurred (250–300 MPa at Tanco vs. 150 MPa at Yichun) (London 1984, 2024; Li et al. 2017). However, a stoichiometric Li end-member of virgilite contains more than 10 times higher Li and Al contents than the calculated Li and Al contents of the quartz-petalite solid solution. Another line of evidence against virgilite as the precursor is that the studied solid solution must have contained some K, as discussed above, which is not present in a virgilite solid solution. Therefore, virgilite cannot be the precursor to the quartz-petalite intergrowths observed in this study. To our knowledge, no naturally occurring mineral solid solutions have been reported with compositions similar to those calculated for the quartz-petalite intergrowths. Such a phase has, however, been reported from an experiment. Sirbescu et al. (2017) synthesized stuffed quartz containing 465–13 240 ppm Li and 1588–51 337 ppm Al by quenching undercooled felsic liquids formed by melting haplogranitic starting materials doped with 4650 ppm Li, 7143 ppm B, and 3–9 wt% H_2O. This phase, if not quenched, was a transient, metastable phase that was readily resorbed by the residual melt. Exsolution did not occur in the experiments of Sirbescu et al. (2017) due to quenching. Such

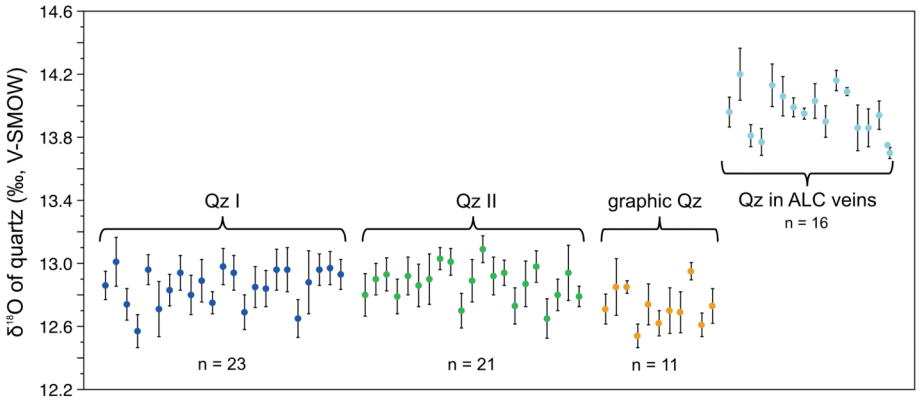

Figure 11. Oxygen isotope values ($\delta^{18}O$‰, 2SE error bars) of Qz I, Qz II, graphic quartz, and quartz from the ALC veins. Qz I, Qz II, and graphic quartz have comparable values, whereas the hydrothermal quartz from the ALC veins has higher values. (Color online.)

experimental results cannot be directly compared to the quartz core at Yichun, but they do demonstrate that a Li- and Al-rich quartz-like solid solution can form from Li-rich granitic melts. Consistent with a stuffed quartz origin for Qz II-b is that the stuffed quartz of Sirbescu et al. (2017) formed euhedral crystals. On balance then, it is more likely that Qz II-b represents exsolution of a metastable stuffed quartz that had initially crystallized from the melt and subsequently unmixed. The remaining melt then crystallized Qz II-c with co-precipitation of petalite. It is possible that some petalite in Qz II-b was the result of co-precipitation, but stuffed quartz that later exsolved and very fine-grained co-precipitates may be indistinguishable based on their mineral textures.

The nature of Qz II as patches or veins in Qz I, where the two generations of quartz are generally characterized by irregular boundaries, resembles typical dissolution and resorption textures (cf. Putnis 2009), indicating that the melt from which Qz II crystallized was out of equilibrium with Qz I. The occurrence of Qz II only inside the core zone suggests that Qz II crystallized from a residual melt that represents the last vestige of pegmatite melt to crystallize in the core. As such, the Qz II-forming melt was more evolved than the Qz I-forming melt and back-reacted with Qz I, with which it was out of equilibrium. The presence of petalite inclusions only in Qz II is consistent with this scenario and suggests that the Qz II-forming melt most likely had significantly higher Li than the earlier melt from which Qz I was formed, thus likely also higher concentrations of other rare elements that are all incompatible in quartz and were residually enriched during crystallization of the core zone.

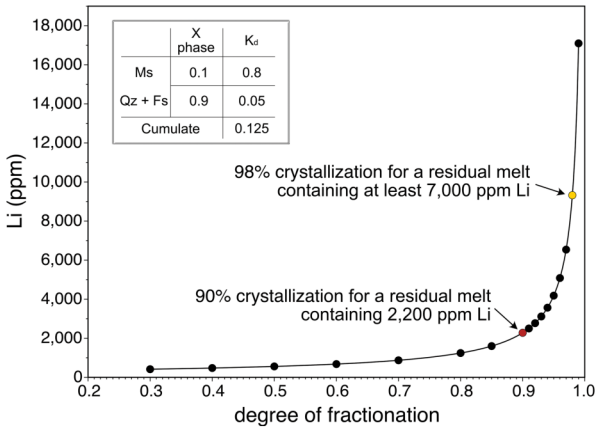

Figure 12. Rayleigh fractionation calculations showing how much mineral fractionation is needed to achieve the lithium concentrations estimated for the pegmatite core zone (Qz II) and measured in the topaz-lepidolite granite, if all Li were concentrated by fractional crystallization alone. The partition coefficients (K_d) of Li between muscovite, feldspar, and quartz, and between peraluminous melts, are adapted from Icenhower and London (1995), Dohmen and Blundy (2014), and Li et al. (2018). X phase = proportion of a mineral phase in the cumulate. (Color online.)

Crystallization of the Last Aliquot of Pegmatite Melt

What remains to be addressed is how this last vestige of melt evolved with respect to the formation of different stages of Qz II and its contained inclusions. Quartz II-a and -b likely crystallized from the same melt as they are always associated with one another, and the initiation of Qz II-b crystallization at euhedral terminations of Qz II-a (Figs. 5a–5c) indicate that Qz II-a was in equilibrium with the Qz II-b melt. As such, Qz II-a and -b likely crystallized from the same melt. Li, Al, P, and most other elements would have increased somewhat in the melt as Qz II-a crystallized, but the residual melt appears to have remained in equilibrium with Qz II-a, as there is no evidence of resorption. Therefore, the melt from which Qz II-a and -b crystallized could have been compositionally similar. The differences in the nature of their contained mineral inclusions may not have been due to radically different melt chemistry, but rather to differences in crystallization kinetics. Quartz II-a grew slowly, as an equilibrium phase, such that Li and Al could diffuse and be concentrated in the residual melt on a local scale. Subsequently, Qz II-b crystallized initially as stuffed quartz, and Qz II-c crystallized, in some cases rapidly, as indicated by plumose-textured, skeletal petalite crystals within quartz. As illustrated in Sirbescu et al. (2017), the formation of stuffed quartz and skeletal minerals requires a more rapid growth than the formation of normal, blocky quartz. Subsequent cooling of the solid solution resulted in the exsolution of petalite and orthoclase/sanidine inclusions. The change of crystallization rate for

Qz II-a and Qz II-b could have reflected undercooling or a change of melt physical properties. The euhedral terminations of Qz II-a in contact with Qz II-b do not suggest significant undercooling, as a change in the degree of undercooling in Li-rich felsic liquids is usually accompanied by disequilibrium mineral boundaries (Maneta 2015; Maneta and Baker 2019). The very similar Ti contents between Qz II-a and -b also support their crystallization at similar temperatures. The presence of fluid inclusions along the edges of Qz II-b cores may indicate that the rapid crystallization observed in this system resulted from volatile saturation and pressure quenching (cf. Bain et al. 2022). Therefore, the transition from Qz II-a to Qz II-b and -c likely resulted from changes in melt physical properties, pressure quenching, or a combination of these factors.

Composition of the Quartz II-Forming Melt

The only Li ore mineral at Yichun documented to date is lepidolite, all of which was interpreted by Wu et al. (2024) to have been formed through secondary replacement in the pegmatite and topaz-lepidolite granite, where it postdates the magmatic mineralogy of both units. The petalite inclusions, which are interpreted here as having formed largely through exsolution (i.e., in Qz II-b) and occasionally via direct crystallization from the Qz II-forming melt (i.e., in Qz II-c), are the first primary lithium aluminosilicate minerals reported at Yichun (Guo et al. 2025; Liu et al. 2025). The question arises as to how the compositions, in particular the Li content calculated for Qz II-b, relate to those of the Qz II-forming melt. The comparison between the stuffed quartz composition of Sirbescu et al. (2017) and the melt composition in their experiments provides some insights into this question: in a run that initially had 4650 ppm Li in the starting melts, the synthesized stuffed quartz yielded an average of 5069 ppm Li. This suggests that the Li content of the Qz II-forming melt should be broadly comparable to the calculated Li concentration in the solid solution that is now unmixed into Qz II-b and its contained inclusions. In addition, because Qz II-b appears to have crystallized from the very last aliquot of melt in the pegmatite (other than the lesser amounts of Qz II-c), the calculated Li content, which, as described above, is 1729–3135 ppm (2200 ppm on average) (Online Materials[1] Table S3) would closely resemble the Li content in the last melt.

Economic Li Mineralization at Yichun

Previous workers have suggested that the Li-muscovite granite and pegmatite were crystallized from melts that share a common magma source at depth (Wu et al. 2018; Pollard 2021; Yin et al. 2022) and that they had evolved to a similar degree as indicated by their comparable compositions, including the Li content of magmatic muscovite (Wu et al. 2024). This conclusion was further used to suggest that the initial Li content of the pegmatite-forming melt was equivalent to the bulk composition of the unaltered Li-muscovite granite, which is also similar to the whole-rock Li content of the zinnwaldite-muscovite granite, assuming a fixed partition coefficient of Li between peraluminous melts and muscovite. If we assume that the primitive pegmatite-forming melt contained an initial Li content of ca. 300 ppm (an average of the published whole-rock Li contents in the Li-muscovite granite) (Huang et al. 2002; Li et al. 2015; Pollard 2021) (Online Materials[1] Table S4), 90% fractional crystallization of the initial pegmatite-forming melt could have generated a residual melt that compositionally resembled the Qz II-forming melt, which contained ~2200 ppm Li (Fig. 12). This is calculated assuming a pegmatite assemblage comprising 10% muscovite plus 90% of equal amounts of quartz and feldspar, which is based on petrological observations of the pegmatite intermediate zone and the Li-muscovite granite (Wu et al. 2018; Pollard 2021) (Online Materials[1] Table S5). This fractional crystallization model is reasonable, as the low viscosity and effective heat convection/crystal segregation in highly evolved, peraluminous pegmatites promote high degrees of mineral fractionation (Bucholz et al. 2023). This model also explains why primary petalite rarely crystallizes in the system, as saturation requires at least 5000 ppm Li (London 1984; Maneta 2015). Because 90% fractional crystallization of a melt with a Li-muscovite granite composition generated the Yichun pegmatite core that is composed almost entirely of quartz, it is not possible that the Li content in the topaz-lepidolite granite (i.e., 7000 ppm on average, up to 1.2 wt%) (Online Materials[1] Table S4) can result from fractional crystallization alone. Recent work on the mineralogy and whole-rock compositions of the topaz-lepidolite granite relative to the underlying granites (Pollard 2021; Yin et al. 2022; Wu et al. 2024) also reached a similar conclusion. In light of this and the occurrence of intense metasomatic Li mineralization as lepidolite-dominant pseudomorphs at Yichun (Wu et al. 2024), approximately more than half of the economic grades of Li in the topaz-lepidolite granite were contributed through metasomatism after the magmatic concentration of 1729–3135 ppm to locally ≤5000 ppm Li.

Implications

The core zone of the pegmatite at the giant Yichun Li-Cs-Ta-Nb deposit consists almost entirely of quartz, in which magmatic Qz I dominates. Abundant petalite and lesser orthoclase/sanidine occur as globular to vermicular inclusions in a second generation of magmatic quartz (Qz II) that variably resorbed Qz I. Quartz II crystallized from the most evolved, final aliquot of pegmatite melt. Quartz II is characterized by three successive stages of growth, commencing with intergrowths of micrographic orthoclase/sanidine inclusions in Qz II-a, subsequent crystallization of Li- and Al-rich stuffed quartz (Qz II-b), which is the most abundant variety of Qz II, and eventually Qz II-c that was co-precipitated with its contained petalite inclusions. We report, for the first time, to our knowledge, petalite-quartz intergrowths that formed via exsolution from a solid solution in nature. This solid solution resembles Li-, Al-rich stuffed quartz, reported previously in quenching experiments of Li-doped granitic melts. The consistent proportion of petalite in Qz II-b underlines the possibility of using this quartz-petalite solid-solution composition as a geothermometer, which will be an avenue for future investigations. Petalite inclusions within Qz II-c, on the other hand, are interpreted as direct crystallization with quartz, and their variable sizes and textures are consistent with the variable development of Ostwald ripening at different growth rates. Rayleigh fractionation calculations suggest that 90% fractionation can ultimately enrich Li to

~2200 ppm in the most evolved melt of the Yichun granite-pegmatite system. This Li abundance is consistent with image-analysis-based mass-balance calculations of the Li content in the melt that formed the final crystallization products in the core zone (Qz II). However, it is many times lower than the Li content reported for the Li-mineralized, underlying topaz-lepidolite granite, which shares the same magma source as the pegmatite. Therefore, fractional crystallization alone cannot account for the high Li content in the topaz-lepidolite granite, and processes such as metasomatism must have played a crucial role (Wu et al. 2024). Our study supports that the economic grade of Li mineralization in peraluminous granites from South China and potentially elsewhere cannot be formed via magmatic evolution alone. The hypothesis that pegmatites can act as permeability barriers to metasomatizing fluids (cf. Guo et al. 2024) is consistent with the intense metasomatism-driven Li mineralization observed at Yichun and other South China rare-metal granites. Though validation of this hypothesis calls for further evidence, peraluminous granites capped by older pegmatite sheets may theoretically present targets for future exploration of lithium.

Acknowledgments and Funding

We are grateful to Fuyuan Wu, Jiankang Li, Alan Anderson, and Daniel Kontak for discussions on the origin of pegmatites and the significance of primary lithium aluminosilicates in pegmatites. Xiaochao Che, Ke Geng, Dapeng Li, Sharon Lackie, and Melissa Price are appreciated for their help during lab work. The manuscript benefited significantly from reviews by Mona-Liza Sirbescu, Lot Koopmans, and an anonymous reviewer. The study was funded by two National Natural Science Foundation of China (NSFC) grants (Nos. 92462302 and 42403065), an Open Research Project from the State Key Laboratory of Geological Processes and Mineral Resources (China University of Geosciences), two Open Research Projects from Shandong Provincial Lunan Geology and Exploration Institute and Shandong Engineering Research Center of Rare Elements Exploration and Comprehensive Utilization (LNY202301, LNY202302), China-CEEC Universities Joint Education Program (2022177), the Frontiers Science Center for Deep-time Digital Earth (2652023001), the Key Laboratory of Gold Mineralization Processes and Resource Utilization Subordinated to the Ministry of Natural Resources, the Open Research Project from the State Key Laboratory of Critical Earth Material Cycling and Mineral Deposits, Nanjing University (No. 2025-K16), and the Shandong Key Laboratory of Metallogenic Geological Process and Resources Utilization (No. KFKT202403).

References Cited

Bain, W.M., Lecumberri-Sanchez, P., Marsh, E.E., and Steele-MacInnis, M. (2022) Fluids and melts at the magmatic-hydrothermal transition, recorded by unidirectional solidification textures at Saginaw Hill, Arizona, USA. Economic Geology and the Bulletin of the Society of Economic Geologists, 117, 1543–1571, https://doi.org/10.5382/econgeo.4952.

Baker, D.R., Sirbescu, M.-L., Maneta, V., Webber, K.L., and Simmons, W.B. (2018) Quantitative analysis of natural and experimental graphic textures. Canadian Mineralogist, 56, 625–643, https://doi.org/10.3749/canmin.1700084.

Ballouard, C., Poujol, M., Boulvais, P., Branquet, Y., Tartèse, R., and Vigneresse, J.-L. (2016) Nb-Ta fractionation in peraluminous granites: A marker of the magmatic-hydrothermal transition. Geology, 44, 231–234, https://doi.org/10.1130/G37475.1.

Ballouard, C., Massuyeau, M., Elburg, M.A., Tappe, S., Viljoen, F., and Brandenburg, J.-T. (2020) The magmatic and magmatic-hydrothermal evolution of felsic igneous rocks as seen through Nb-Ta geochemical fractionation, with implications for the origins of rare-metal mineralizations. Earth-Science Reviews, 203, 103115, https://doi.org/10.1016/j.earscirev.2020.103115.

Bowell, R.J., Lagos, L., De Los Hoyos, C.R., and Declercq, J. (2020) Classification and characteristics of natural lithium resources. Elements, 16, 259–264, https://doi.org/10.2138/gselements.16.4.259.

Bradley D.C., McCauley A.D., and Stillings L.M. (2017) Mineral-Deposit Model for Lithium-Cesium-Tantalum Pegmatites. U.S. Geological Survey, Scientific Investigations Report 2010–5070–O, 48 p. USGS.

Breasley, C.M., Martins, T., Linnen, R.L., Deveau, C., Groat, L.A., Koopmans, L., Landry, E., and Moser, D. (2025) The geochemistry, origins and metallurgical implications of different textural types of spodumene-quartz intergrowths (SQUI) from the Tanco pegmatite, Manitoba, Canada. Ore Geology Reviews, 180, 106577, https://doi.org/10.1016/j.oregeorev.2025.106577.

Breiter, K., Müller, A., Leichmann, J., and Gabašová, A. (2005) Textural and chemical evolution of a fractionated granitic system: The Podlesí stock, Czech Republic. Lithos, 80, 323–345, https://doi.org/10.1016/j.lithos.2003.11.004.

Brown, W.L. and Parsons, I. (1989) Alkali feldspars: Ordering rates, phase transformations and behaviour diagrams for igneous rocks. Mineralogical Magazine, 53, 25–42, https://doi.org/10.1180/minmag.1989.053.369.03.

Bucholz, C.E., Anbar, A., and Weis, D. (2023) The diversity and origin of granites. In A. Anbar and D. Weis, Eds., Treatise in Geochemistry, 3rd edition, p. 153–202. Elsevier.

Černý, P., Blevin, P.L., Cuney, M., and London, D. (2005) Granite-related ore deposits. Society of Economic Geologists 100th Anniversary Volume, 337–370.

Černý, P., London, D., and Novak, M. (2012) Granitic pegmatites as reflections of their sources. Elements, 8, 289–294, https://doi.org/10.2113/gselements.8.4.289.

Che, X., Wu, F., Wang, R., Gerdes, A., Ji, W., Zhao, Z., Yang, J., and Zhu, Z. (2015) In situ U-Pb isotopic dating of columbite-tantalite by LA-ICP-MS. Ore Geology Reviews, 65, 979–989, https://doi.org/10.1016/j.oregeorev.2014.07.008.

Diao, X., Wu, M., Zhang, D., and Liu, J. (2022) Textural features and chemical evolution of Ta-Nb-W-Sn oxides in the Jianfengling Deposit, South China. Ore Geology Reviews, 142, 104690, https://doi.org/10.1016/j.oregeorev.2021.104690.

Diao, X., Wu, M., Qiu, K., Zhang, R., Zou, S., and Zhang, D. (2024) The role of magmatic versus metasomatic processes in Ta-Nb mineralization at the Jiabusi Deposit, Inner Mongolia: Evidence from textural and chemical features of rare metal minerals and mica. Ore Geology Reviews, 165, 105871, https://doi.org/10.1016/j.oregeorev.2024.105871.

Dittrich, T., Seifert, T., Schulz, B., Hagemann, S., Gerdes, A., and Pfänder, J. (2019) Archean Rare-Metal Pegmatites in Zimbabwe and Western Australia: Geology and Metallogeny of Pollucite Mineralisations, 125 p. Springer.

Dohmen, R. and Blundy, J. (2014) A predictive thermodynamic model for element partitioning between plagioclase and melt as a function of pressure, temperature and composition. American Journal of Science, 314, 1319–1372, https://doi.org/10.2475/09.2014.04.

Downs, R.T. (2006) The RRUFF project: An integrated study of the chemistry, crystallography, Raman and infrared spectroscopy of minerals. In Program and Abstracts of the 19th General Meeting of the International Mineralogical Association, p. 13. International Mineralogical Association.

Fenn, P.M. (1986) On the origin of graphic granite. American Mineralogist, 71, 325–330.

French, B.M. (1978) Virgilite: A new lithium aluminum silicate mineral from the Macusani glass, Peru. American Mineralogist, 63, 461–465.

Frost, R.L., Xi, Y., Scholz, R., López, A., Belotti, F.M., and Chaves, M.L.S.C. (2013) Raman and infrared spectroscopic characterization of the phosphate mineral lithiophilite—$LiMnPO_4$. Phosphorus, Sulfur, and Silicon and the Related Elements, 188, 1526–1534, https://doi.org/10.1080/10426507.2012.761985.

Guo, C., Zhang, B., Zheng, Y., Xu, J., Zhao, Q., Yan, J., Zhou, R., Fu, W., and Huang, K. (2024) Granite-type lithium deposits in China: Important characteristics, metallogenic conditions, and genetic mechanism. Yanshi Xuebao, 40, 347–403, https://doi.org/10.18654/1000-0569/2024.02.02 (in Chinese with English abstract).

Guo, B., Zhao, K., Liu, G., Liu, H., Chen, W., Jiang, S., and Yaxley, G.M. (2025) Intense magmatic differentiation of the Yashan rare-metal granites in South China: Insights from geochemistry of Li-bearing minerals. Lithos, 518–519, 108322, https://doi.org/10.1016/j.lithos.2025.108322.

Harlaux, M., Mercadier, J., Bonzi, W.M.-E., Kremer, V., Marignac, C., and Cuney, M. (2017) Geochemical signature of magmatic-hydrothermal fluids exsolved from the beauvoir rare-metal granite (Massif Central, France): Insights from LA-ICP-MS Analysis of Primary Fluid Inclusions. Geofluids, 2017, 1–25, https://doi.org/10.1155/2017/1925817.

Hou, Z., Fusseis, F., Schöpfer, M., and Grasemann, B. (2023) Synkinematic evolution of stylolite porosity. Journal of Structural Geology, 173, 104916, https://doi.org/10.1016/j.jsg.2023.104916.

Hou, Z., Qiu, K., Zhou, T., and Cai, Y. (2024) An advanced image processing technique for backscatter-electron data by scanning electron microscopy for microscale rock exploration. Journal of Earth Science, 35, 301–305, https://doi.org/10.1007/s12583-024-1969-9.

Huang, R. and Audétat, A. (2012) The titanium-in-quartz (TitaniQ) thermobarometer: A critical examination and re-calibration. Geochimica et Cosmochimica Acta, 84, 75–89, https://doi.org/10.1016/j.gca.2012.01.009.

Huang, X., Wang, R., Chen, X., Hu, H., and Liu, C. (2002) Vertical variations in the mineralogy of the Yichun topaz lepidolite granite, Jiangxi province, southern China. Canadian Mineralogist, 40, 1047–1068, https://doi.org/10.2113/gscanmin.40.4.1047.

Icenhower, J. and London, D. (1995) An experimental study of element partitioning among biotite, muscovite, and coexisting peraluminous silicic melt at 200 MPa (H_2O). American Mineralogist, 80, 1229–1251, https://doi.org/10.2138/am-1995-11-1213.

Kerr, A. (2023) Critical minerals in the context of Canada: Concepts, challenges and contradictions. Geoscience Canada, 50, 85–103, https://doi.org/10.12789/geocanj.2023.50.199.

Kesler, S.E., Gruber, P.W., Medina, P.A., Keoleian, G.A., Everson, M.P., and Wallington, T.J. (2012) Global lithium resources: Relative importance of pegmatite, brine and other deposits. Ore Geology Reviews, 48, 55–69, https://doi.org/10.1016/j.oregeorev.2012.05.006.

Li, J., Huang, X., He, P., Li, W., Yu, Y., and Chen, L. (2015) In situ analyses of micas in the Yashan granite, South China: Constraints on magmatic and hydrothermal evolutions of W and Ta-Nb bearing granites. Ore Geology Reviews, 65, 793–810, https://doi.org/10.1016/j.oregeorev.2014.09.028.

Li, S., Li, J., Chou, I.M., Jiang, L., and Ding, X. (2017) The formation of the Yichun Ta-Nb deposit, South China, through fractional crystallization of magma indicated by fluid and silicate melt inclusions. Journal of Asian Earth Sciences, 137, 180–193, https://doi.org/10.1016/j.jseaes.2016.11.016.

Li, J., Huang, X., Wei, G., Liu, Y., Ma, J., Han, L., and He, P. (2018) Lithium isotope fractionation during magmatic differentiation and hydrothermal processes in rare-metal granites. Geochimica et Cosmochimica Acta, 240, 64–79, https://doi.org/10.1016/j.gca.2018.08.021.

Lin, D. (1996) Tantalum-rich Granite Type Deposits in South China. Geological Publishing House (in Chinese).

Linnen, R.L. and Cuney, M. (2008) Granite-related rare-element deposits and experimental constraints on Ta-Nb-W-Sn-Zr-Hf mineralization. In R.L. Linnen and I.M. Samson, Eds., Rare-Element Geochemistry and Mineral Deposits, 17, Short Course Notes, p. 45–67. Geological Association of Canada.

Litasov, K.D. and Podgornykh, N.M. (2017) Raman spectroscopy of various phosphate minerals and occurrence of tuite in the Elga IIE iron meteorite. Journal of Raman Spectroscopy, 48, 1518–1527, https://doi.org/10.1002/jrs.5119.

Liu, Z., Li, J., Chen, Z., Zhu, Z., Li, P., Liu, Y., and Han, Z. (2025) The discovery of petalite-bearing granite in the Yashan pluton, Jiangxi Province, China. Bulletin of Mineralogy, Petrology and Geochemistry, 44, 1262–1270 (in Chinese with English abstract).

London, D. (1984) Experimental phase equilibria in the system $LiAlSiO_4$–SiO_2–H_2O: A petrogenetic grid for lithium-rich pegmatites. American Mineralogist, 69, 995–1004.

——— (2008) Pegmatites, 347 p. Canadian Mineralogist Special Publication 10.

——— (2016) Rare-element granitic pegmatites. In P.L. Verplanck and L.W. Hitzman, Eds., Rare Earth and Critical Elements in Ore Deposits, 18, 165–194. Society of Economic Geologists.

——— (2018) Ore-forming processes within granitic pegmatites. Ore Geology Reviews, 101, 349–383, https://doi.org/10.1016/j.oregeorev.2018.04.020.

——— (2024) The Tanco Pegmatite at Bernic Lake Manitoba, Canada. Rocks and Minerals, 99, 60–77, https://doi.org/10.1080/00357529.2023.2253106.

London, D. and Morgan, G.B. (2017) Experimental crystallization of the Macusani Obsidian, with applications to lithium-rich granitic pegmatites. Journal of Petrology, 58, 1005–1030, https://doi.org/10.1093/petrology/egx044.

Lou, F., Shen, W., Wang, D., Shu, L., Wu, F., Zhang, F., and Yu, J. (2005) Zircon U-Pb isotopic chronology of the Wugongshan dome compound granite in Jiangxi Province. Yanshi Xuebao, 79, 636–644 (in Chinese with English abstract).

Maneta, V. (2015) The effect of Li on the petrogenesis of granitic pegmatites, 174 p. Ph.D. thesis, McGill University, Montréal.

Maneta, V. and Baker, D.R. (2019) The potential of lithium in alkali feldspars, quartz, and muscovite as a geochemical indicator in the exploration for lithium-rich granitic pegmatites: A case study from the spodumene-rich Moblan pegmatite, Quebec, Canada. Journal of Geochemical Exploration, 205, 106336, https://doi.org/10.1016/j.gexplo.2019.106336.

Michaud, J.A.-S. and Pichavant, M. (2020) Magmatic fractionation and the magmatic-hydrothermal transition in rare metal granites: Evidence from Argemela (Central Portugal). Geochimica et Cosmochimica Acta, 289, 130–157, https://doi.org/10.1016/j.gca.2020.08.022.

Müller, A., Keyser, W., Simmons, W.B., Webber, K., Wise, M., Beurlen, H., Garate-Olave, I., Roda-Robles, E., and Galliski, M.Á. (2021) Quartz chemistry of granitic pegmatites: Implications for classification, genesis and exploration. Chemical Geology, 584, 120507, https://doi.org/10.1016/j.chemgeo.2021.120507.

Paton, C., Hellstrom, J., Paul, B., Woodhead, J., and Hergt, J. (2011) Iolite: Freeware for the visualisation and processing of mass spectrometric data. Journal of Analytical Atomic Spectrometry, 26, 2508, https://doi.org/10.1039/c1ja10172b.

Pollard, P.J. (2021) The Yichun Ta-Sn-Li deposit, South China: Evidence for extreme chemical fractionation in F-Li-P-rich magma. Economic Geology and the Bulletin of the Society of Economic Geologists, 116, 453–469, https://doi.org/10.5382/econgeo.4801.

Putnis, A. (2009) Mineral Replacement Reactions. Reviews in Mineralogy and Geochemistry, 70, 87–124, https://doi.org/10.2138/rmg.2009.70.3.

Rusiecka, M.K. and Baker, D.R. (2021) Growth and textural evolution during crystallization of quartz and feldspar in hydrous, rhyolitic melt. Contributions to Mineralogy and Petrology, 176, 48, https://doi.org/10.1007/s00410-021-01809-1.

Rusiecka, M.K., Bilodeau, M., and Baker, D.R. (2020) Quantification of nucleation delay in magmatic systems: Experimental and theoretical approach. Contributions to Mineralogy and Petrology, 175, 47, https://doi.org/10.1007/s00410-020-01682-4.

Schneider, C.A., Rasband, W.S., and Eliceiri, K.W. (2012) NIH Image to ImageJ: 25 years of image analysis. Nature Methods, 9, 671–675, https://doi.org/10.1038/nmeth.2089. PubMed https://pubmed.ncbi.nlm.nih.gov/22930834

Simmons, Wm.B. and Webber, K.L. (2008) Pegmatite genesis: State of the art. European Journal of Mineralogy, 20, 421–438, https://doi.org/10.1127/0935-1221/2008/0020-1833.

Sirbescu, M.-L., Schmidt, C., Veksler, I.V., Whittington, A.G., and Wilke, M. (2017) Experimental crystallization of undercooled felsic liquids: Generation of pegmatitic texture. Journal of Petrology, 58, 539–568, https://doi.org/10.1093/petrology/egx027.

Wei, P., Geng, K., Liu, J., Zhang, Y., Li, D., Cai, N., Zhang, C., Liu, Q., and Xie, W. (2024) Oxygen isotope in situ microanalysis of zircon by SHRIMP V. Rock and Mineral Analysis, 43, 723–733 (in Chinese with English abstract).

Wu, M., Samson, I.M., and Zhang, D. (2017) Mineralogical and geochemical constraints on the nature of granite-hosted W mineralization at the Dajishan W-Ta-Nb deposit, Nanling Range, SE China. Economic Geology and the Bulletin of the Society of Economic Geologists, 112, 855–887, https://doi.org/10.2113/econgeo.112.4.855.

——— (2018) Textural features and chemical evolution in Ta-Nb oxides: Implications for deuteric rare-metal mineralization in the Yichun granite-marginal pegmatite, southeastern China. Economic Geology and the Bulletin of the Society of Economic Geologists, 113, 937–960, https://doi.org/10.5382/econgeo.2018.4577.

Wu, M., Diao, X., Samson, I.M., and Zheng, X. (2024) Role of metasomatism in formation of the Yichun rare-metal deposit, China. Ore Geology Reviews, 174, 106297, https://doi.org/10.1016/j.oregeorev.2024.106297.

Yin, L., Pollard, P.J., Hu, S., and Taylor, R.G. (1995) Geologic and geochemical characteristics of the Yichun Ta-Nb-Li deposit, Jiangxi Province, South China. Economic Geology and the Bulletin of the Society of Economic Geologists, 90, 577–585, https://doi.org/10.2113/gsecongeo.90.3.577.

Yin, R., Huang, X., Wang, R., Sun, X., Tang, Y., Wang, Y., and Xu, Y. (2022) Rare-metal enrichment and Nb-Ta fractionation during magmatic-hydrothermal processes in rare-metal granites: Evidence from zoned micas from the Yashan Pluton, South China. Journal of Petrology, 63, egac093, https://doi.org/10.1093/petrology/egac093.

Zhu, J., Li, R., Li, F., Xiong, L., Zhou, F., and Huang, X. (2001) Topaz-albite granites and rare-metal mineralization in the Limu District, Guangxi Province, southeast China. Mineralium Deposita, 36, 393–405, https://doi.org/10.1007/s001260100160.

Zhu, Z., Wang, R., Che, X., Zhu, J., Wei, X., and Huang, X. (2015) Magmatic-hydrothermal rare-element mineralization in the Songshugang granite (northeastern Jiangxi, China): Insights from an electron-microprobe study of Nb-Ta-Zr minerals. Ore Geology Reviews, 65, 749–760, https://doi.org/10.1016/j.oregeorev.2014.07.021.

Zhu, Z., Wang, R., Marignac, C., Cuney, M., Mercadier, J., Che, X., and Lespinasse, M.Y. (2018) A new style of rare metal granite with Nb-rich mica: The Early Cretaceous Huangshan rare-metal granite suite, northeast Jiangxi Province, southeast China. American Mineralogist, 103, 1530–1544, https://doi.org/10.2138/am-2018-6511.

Manuscript received March 8, 2025
Manuscript accepted June 15, 2025
Accepted manuscript online June 25, 2025
Manuscript Handled by Mona Sirbescu

Endnotes:

[1]Deposit item AM-26-29818. Online Materials are free to all readers. Go online, via the table of contents or article view, and find the tab or link for supplemental materials.